

# South Island West Coast orographic rainfall – a polarimetric radar view

J. F. Crouch<sup>1</sup> and F. M. Russell<sup>1</sup>

<sup>1</sup>Meteorological Service of New Zealand (MetService), P.O. Box 722, Wellington, New Zealand

Correspondence: john.crouch@metservice.com

**Key words:** orographic rainfall, polarimetric radar, trapped mountain waves, turbulence as a mechanism to enhance orographic rainfall, Southern Alps

---

## Abstract

This study uses a dual-polarisation C-band weather radar to investigate a period of heavy orographic rainfall about the South Island West Coast on 18 June 2015 when rainfall rates of 20-35+ mm/h were recorded from stratiform rain with no embedded convection. The dual-polarisation imagery clearly shows the location and depth of the melting layer and Dendritic Snow Growth Zone (DGZ), which are both more intense over the mountains, and shows enhancement of rainfall below the melting layer due to collision-coalescence and collectional growth (e.g. seeder-feeder) type effects. Radar doppler radial velocity imagery reveals an embedded trapped mountain wave turbulent layer about 1-2 km thick immediately above the mountains which has not been observed before in New Zealand radar imagery. The moist onshore winds are initially lifted by a low-level barrier jet, then are lifted further above the observed mountain wave turbulent layer providing moisture to the DGZ and enhancing ice growth in this zone immediately above, and slightly upwind, of the mountains. Specific Differential Phase ( $K_{DP}$ ) imagery reveals an additional ice-growth layer between the DGZ and the melting layer. It is suggested this may be an ice splintering and riming zone, and that the turbulent layer below is producing higher concentrations of super-cooled liquid water leading to enhanced riming in this zone. The turbulent trapped mountain wave layer therefore appears to be an important mechanism in enhancing the surface rainfall by providing additional lift to the onshore airmass, enhancing ice crystal growth aloft and, when combined with warm rain collision-coalescence and collectional growth processes, appears to shift the maximum rainfall upwind towards the first range of mountains.

## 1. Introduction

The west coast of the South Island is the wettest part of New Zealand with an average annual rainfall of 2,000-3,000mm about the coast, and greater than 8,000 to 10,000mm about the ranges of the Southern Alps (Macara, 2018). Heavy rainfall events are common, and often exceed 100mm in a 24-hour period, with significant spill-over into the headwaters of the main Canterbury and Otago lakes and rivers.

Several New Zealand studies have investigated Southern Alps rainfall, mainly concentrating on the distribution of rainfall across the Southern Alps and spillover into the catchments east of the main divide (e.g., Sinclair et al., 1997, Chater and Sturman, 1998, Henderson and Thompson, 1999, Purdy and Austin, 2003). The largest of these studies was the multi-agency Southern Alps Experiment (SALPEX) in the mid 1990's (Wratt et al., 1996). This was a large multi-faceted study into the influence of the mountains on the distribution of rain

and snow fall across the Southern Alps. Observational data was obtained through a combination of local weather stations, rain-gauges, balloon flights, satellite data and research aircraft measurements, but radar observations were limited to an operational MetService C-band single polarisation radar on the Canterbury Plains located about 115 km southeast of the Southern Alps main divide, and two small mobile X-band radars on the West Coast (Purdy et al., 2005).

Of the numerous papers that came from the SALPEX experiment, three are relevant to this study. Sinclair et al. (1997) used rain gauge, radar and atmospheric observations to study a prolonged northwesterly storm which affected the South Island West Coast and Southern Alps in November 1994. During this storm the location and intensity of precipitation varied markedly, mainly dependent on stability. They suggested that in stable blocked northwesterly flows, the ascent and precipitation maxima are shifted upstream of the Southern Alps main divide, while spillover is enhanced during stronger and/or unstable flows as the upstream influence lessens and snow/ice particles drift farther downwind before falling below the freezing level. Revell et al. (2001) modelled the northeast barrier flow which occurs along the West Coast in stable prefrontal northwesterly flows. Their modelling showed that for the case studied, the barrier jet extended offshore and provided a gradual uplift to the onshore flow which extended far enough upstream to enable cloud droplets to grow to drizzle droplets before reaching the more substantial updrafts at the foot of the Southern Alps. They suggested this allows vigorous prefrontal precipitation to occur over the foothills and mountains due largely to warm rain processes. Purdy et al. (2005) used 2 X-band radars to document a seeder-feeder event on the windward side of the Southern Alps where precipitation in the form of snow falling from a cloud sheet aloft enhanced rainfall at lower levels.

More recently, several international studies investigating the microphysical processes associated with orographic

rainfall have shown that turbulence plays an important role in increasing surface precipitation by enhancing snow crystal growth aloft. Houze and Medina (2005) used S-band radar data over the Oregon Cascade mountains (USA) and European Alps to show that turbulent cells embedded within a precipitating orographic cloud system made possible a precipitation growth mechanism that would not have been present in a laminar upslope flow. They showed that the turbulent updraft cells create pockets of highly concentrated super-cooled liquid water which leads to increased riming of dendritic snow crystals and flakes falling from above. This produces heavier, more rapidly falling precipitation particles which have a higher probability of reaching the ground upwind of a mountain crest. Without the turbulent cells, condensate would more likely be advected farther up and perhaps even over the mountain range. Geerts et al. (2011) showed similar results from a study of 10 winter storms over the Medicine Bow Range in Wyoming USA. They noted that Doppler vertical velocity transects showed an approximately 1 km deep turbulent layer draped over the terrain which was sometimes clearly distinct from the stratified flow in the free troposphere aloft, and that rapid snow growth was observed within the boundary layer turbulence, especially when it was more intense. They also suggested that boundary layer turbulence may also be important in warm clouds through accelerated growth by collision and coalescence. Grazioli et al. (2015) used a polarimetric X-band radar in the Swiss Alps to observe the polarimetric radar signatures associated with riming and snowfall microphysics. They also investigated the role of turbulence in enhancing snow crystal growth and noted when a turbulent atmospheric layer persists for several hours and ensures continuous super-cooled liquid water generation, riming can be sustained longer and large accumulations of snow at ground level can be generated. Aikins et al. (2016) used a suite of high-resolution radars to study winter orographic storms over the Sierra Madre Range in Wyoming USA. Although cloud liquid water was absent, a turbulent shear layer created by a mid-level cross-barrier jet still enhanced snow growth through deposition and aggregation processes.

This study will use a dual-polarisation C-band weather radar to investigate a South Island West Coast orographic heavy rainfall event on 18 June 2015. This event is of interest as it was a stable stratiform rain event with no embedded convection yet still produced prolonged heavy rainfall rates of 20-30+ mm/h near the radar well upwind of the main divide (similar to the observation made by Sinclair et al. (1997)). The study will show how the radar imagery can be used to identify some of the mesoscale and microphysical processes involved in producing the heavy stratiform rain, and also show the role that trapped mountain waves embedded within the rain-band may be playing in enhancing surface precipitation.

## 2. MetService Westland weather radar

The New Zealand Meteorological Service (MetService) Westland weather radar is a Vaisala WRM200 dual polarisation C-band Doppler radar. It was installed in November 2011 and is located about 8 km east of Hokitika (Figure 1) at a height of 360 metres above mean

sea level (amsl). The radar produces three dimensional scans out to 250 km range every 7.5 minutes. The scans contain 13 elevation angles from 0.5° to 20.0° with a range bin spacing of 200 metres. The lowest radar beams are blocked significantly by the western ranges of the Southern Alps about 15 km east of the radar, which does affect surface rainfall estimates in this area. The radar beams are however unobstructed in this same direction from 3.0° degrees and higher which allows good radar coverage over the Southern Alps from about 1.3 km to 20 km amsl. The radar beams are unobstructed in all other directions from southwest to north-northeast of the radar. This allows excellent radar coverage of weather systems approaching from the west.

The radar produces the following radar fields:

- Reflectivity (horizontal -  $Z_H$ ) – dependent on the size and density of radar targets.
- Doppler Radial Velocity ( $V$ ) - Nyquist Velocity

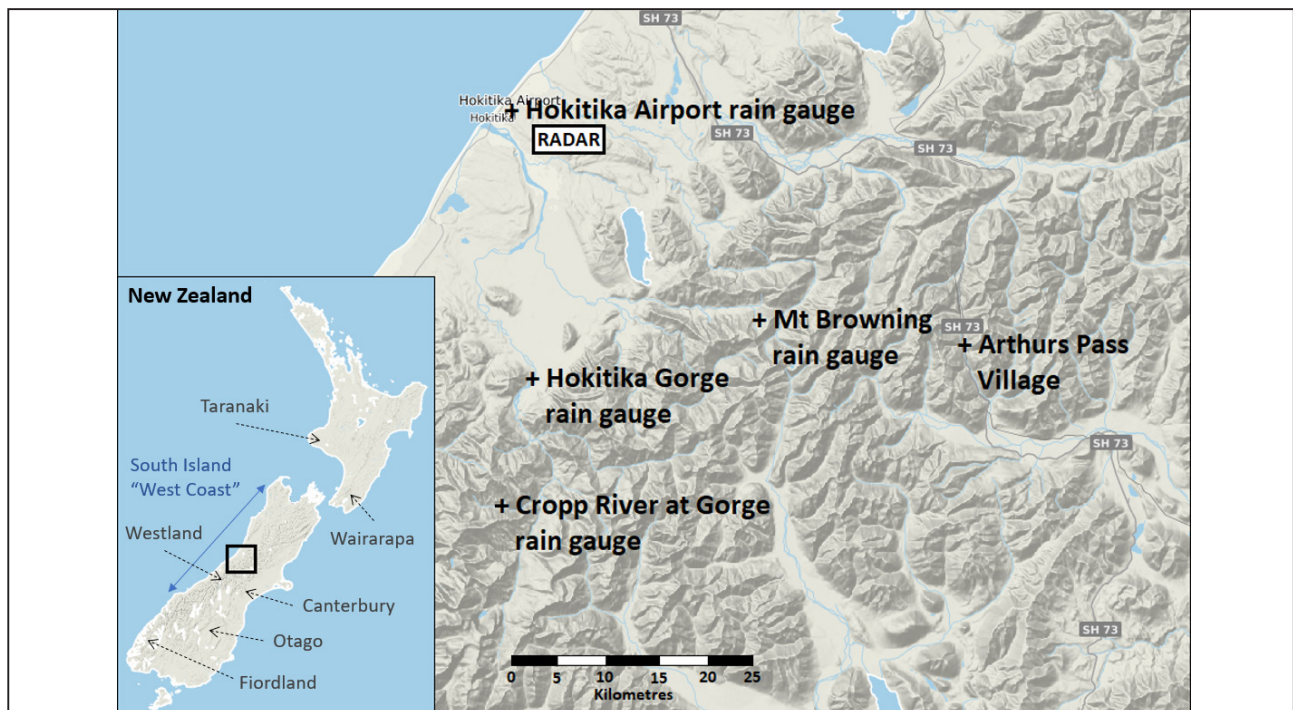


**Figure 1:** Map showing the study area near Hokitika on the South Island west coast of New Zealand, and locations mentioned in the text. The location of the MetService Westland weather radar (marked as RADAR) and the rain-gauges mentioned in this study are marked on the larger map. The main divide of the Southern Alps lies approximately midway between the Mt Browning rain-gauge and Arthurs Pass village.

is 16 m/s, obtained using dual pulse-repetition-frequencies of 600 and 400Hz. The data can be unfolded in post-processing using Vaisala IRIS radar software.

- Differential Reflectivity ( $Z_{DR}$ ) – dependent on the shape of a radar target.
- Correlation Coefficient ( $\rho_{HV}$ ) – a measure of radar target diversity.
- Differential Phase ( $\phi_{DP}$ ) and Specific Differential Phase ( $K_{DP}$ ) – dependent on the shape and density of radar targets.
- Hydrometeor Classification - A fuzzy logic algorithm which uses the radar fields to classify targets into 5 meteorological and 1 non-meteorological categories.

### 3. Heavy orographic stratiform rainfall event – 18 June 2015

A major frontal system affected the South Island of New Zealand on 18 and 19 June 2015, bringing heavy rain to the South Island West Coast and Southern Alps, and low-level snow to parts of Canterbury, Otago and Southland.

Rain was particularly heavy about Westland and the Southern Alps, with over 500mm being recorded at several stations in the 42 hours between 6am on the 18th and midnight on the 19th NZST (West Coast Regional Council gauges - Cropp River at Gorge 537mm, Mt Browning 533mm and Hokitika Gorge 513mm. Location of gauges shown in Figure 1). This system then brought heavy rain to the lower North Island over the following 2 days with significant flooding of rivers and streams from Taranaki to Wairarapa.

This study will consider the 12-hour period from midday to midnight on 18 June 2015 NZST (18/0000 to 18/1200 UTC) and examine the rainfall near the MetService Westland weather radar sited near Hokitika (Figure 1). This event is of interest as it produced rainfall rates of 20-30+ mm/h from stratiform precipitation with no embedded convection. The heaviest rainfall was observed well upstream of the Southern Alps main divide at the Hokitika Gorge and Cropp River at Gorge gauges, with lesser amounts recorded near the main divide at the Mt Browning gauge.

The heavy rain on the South Island West Coast occurred ahead of a cold front which moved slowly northwards over the South Island during 18 June 2015 (Figure 2).

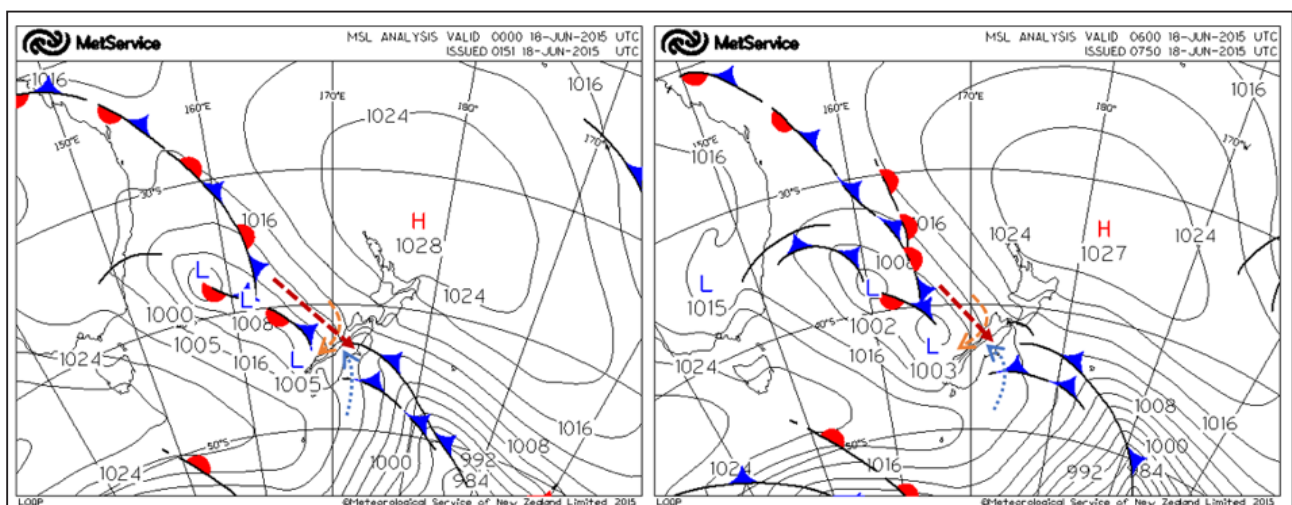


**Figure 2:** Mean sea level pressure analysis for 00:00 UTC (Midday NZST) 18 June 2015 on left and 06:00 UTC (6pm NZST) 18 June 2015 on right. Dashed arrows indicate wind flow around the South Island of New Zealand - Orange is the low-level northeasterly barrier flow on the West Coast, Red is the deeper northwesterly flow aloft (which crosses the Southern Alps), and Blue indicates a low-level southerly about Canterbury.

A warm, moist, and deep northwesterly airflow overlaid a coastal north to northeasterly barrier flow (Figure 3), and this was associated with a well-defined atmospheric river extending from the Coral Sea (east of Queensland Australia) to the South Island West Coast (Figure 4). A low level northwesterly wind speed maximum of around 26m/s (50kt) was observed over the radar at a height of about 2.5km amsl during the afternoon (Figure 5a), but this later evolved into a better defined, but similar strength, low-level jet centred just above the barrier flow at a height of about 1.5km amsl by early evening (Figure 5b). A tephigram for Hokitika Airport (Figure 6) derived from the MetService 8km WRF model initialised off the US NCEP/GFS global model shows a deeply stable atmosphere with the strongest vertical motion between 1 and 3 km high immediately above the northeast

barrier flow. Low level (925-850hPa) wet-bulb potential temperature was around 12°C.

Figure 7 shows a 12-hour gauge corrected radar rainfall accumulation from the MetService Westland radar for the period from midday to midnight NZST (00:00 to 12:00 UTC) 18 June 2015, along with the locations of the MetService Westland radar and the Hokitika Aero, Hokitika Gorge and Mt Browning rain gauges. The image shows a significant enhancement of rainfall just inland from the coast around the radar site, but the rainfall estimates are significantly blocked east of the radar due to terrain and are therefore underestimated in this area. Also depicted on the image is a line showing the transect of vertical radar cross-sections presented in this study.

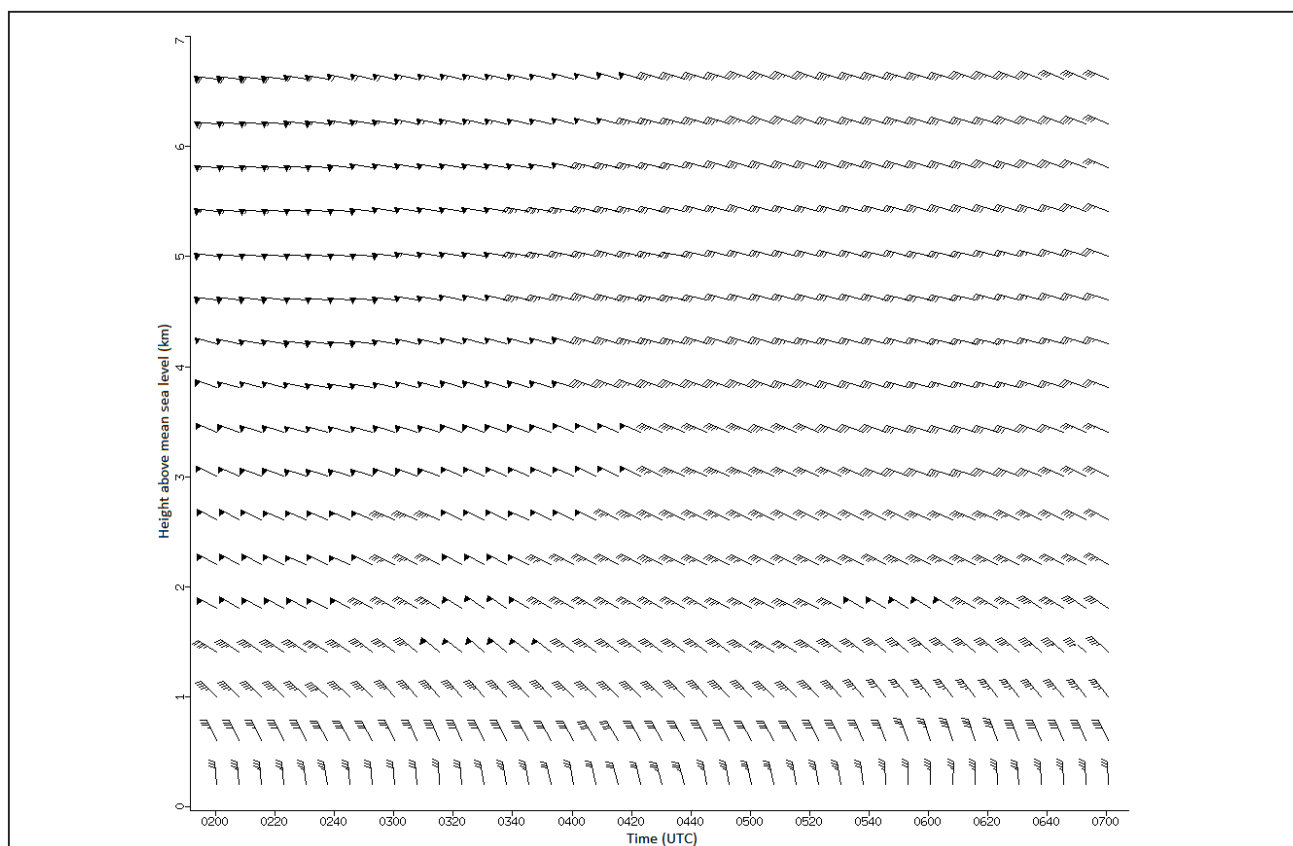


**Figure 3:** Vertical wind profile derived from the MetService Westland weather radar between 02:00 UTC (2pm NZST) and 07:00 UTC (7pm NZST) 18 June 2015. The wind profiles are calculated every 7.5 minutes using a Volume Velocity Processing technique (Waldteufel and Corbin, 1979), using data within 30km range from the radar. The profile shows a generally deep and uniform northwesterly flow aloft, with winds veering to a strong north to northeasterly barrier flow below 1km. Plotted wind barbs are in knots.

The hourly rainfall intensities and 12-hour rainfall totals for the Hokitika Airport, Hokitika Gorge and Mt Browning rain gauges, along with their height above mean sea level, are shown in Figure 8. These gauges have been chosen as they are located near the MetService Westland radar. The heaviest rain was recorded well upstream, about 20km west of the Southern Alps main

divide, at Hokitika Gorge with consistent rainfall rates of 20-30+ mm/h in the 7 hours between midday and 7pm NZST (0000 to 0700 UTC) 18 June 2015. Hourly rainfall rates were less at the Mt Browning gauge located close to the main divide, however both gauges recorded their highest rainfall rates between 5 and 7pm NZST.

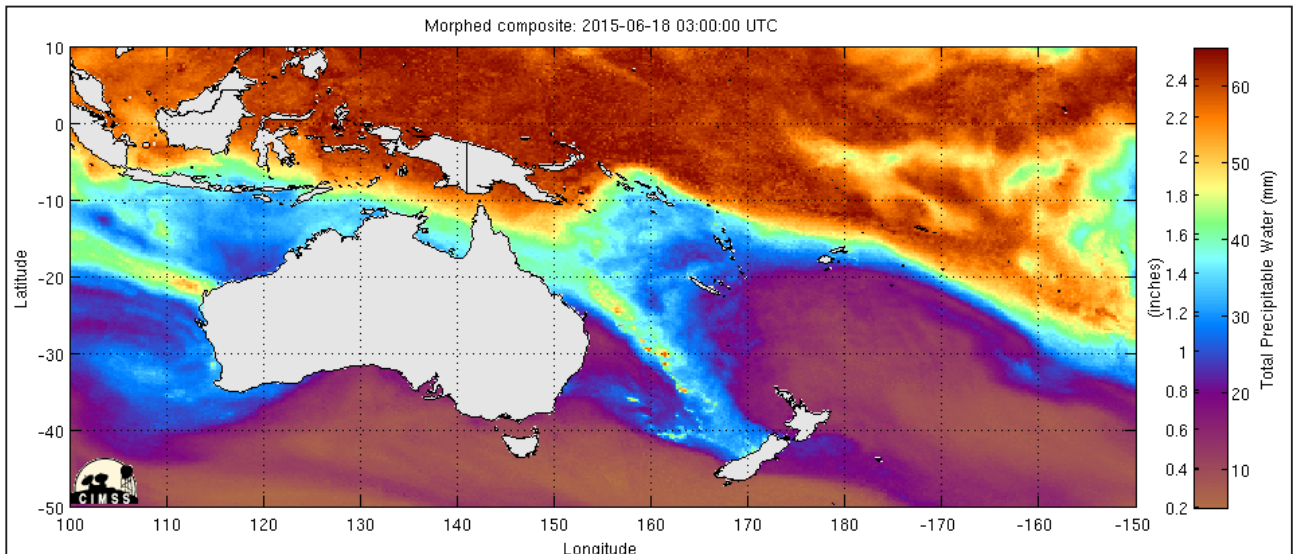


**Figure 4:** Total Precipitable Water image for 03:00 UTC (3pm NZST) 18 June 2015 from Cooperative Institute for Meteorological Satellite Studies (CIMSS) showing an atmospheric river (of moisture) extending from the Coral Sea onto the South Island of New Zealand.

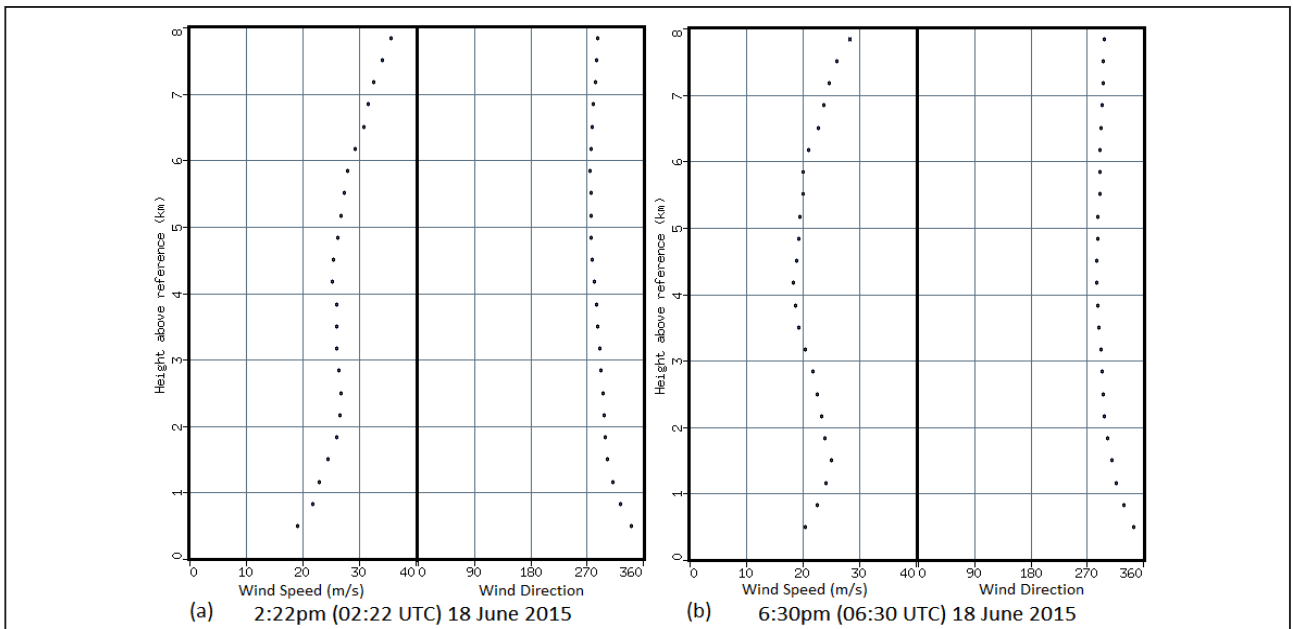


**Figure 5:** Vertical profile of wind speed and direction derived from the MetService Westland weather radar at (a) 02:22 UTC (2:22pm NZST) and (b) 06:30 UTC (6:30pm NZST) 18 June 2015. The profiles are calculated using a Volume Velocity Processing technique (Waldeufel and Corbin, 1979), using data within 30km range from the radar.

#### 4. Polarimetric radar cross-sections

Radar vertical cross-sections for two times, approximately three hours apart, during the period of heavy rain between midday and midnight (NZST) on 18 June 2015 will now be discussed. This period is of interest as very heavy rainfall rates were recorded from stratiform rain with no embedded convection, and the heaviest rain recorded was about 20km upwind of the main divide at the Hokitika Gorge gauge. The cross-sections are all

along the same line which is orientated in a northwest to southeast direction (see Figure 7), and this is chosen to align with the prevailing northwest flow aloft (see Figures 3 and 5). The radar cross-sections pass through Hokitika (northwest of the radar) and Arthurs Pass village (southeast of the radar), which are both marked on the imagery. The cross-sections extend to 60 km away from the radar in both directions, extend from sea level up to 10 km high, and are overlaid with a terrain profile.

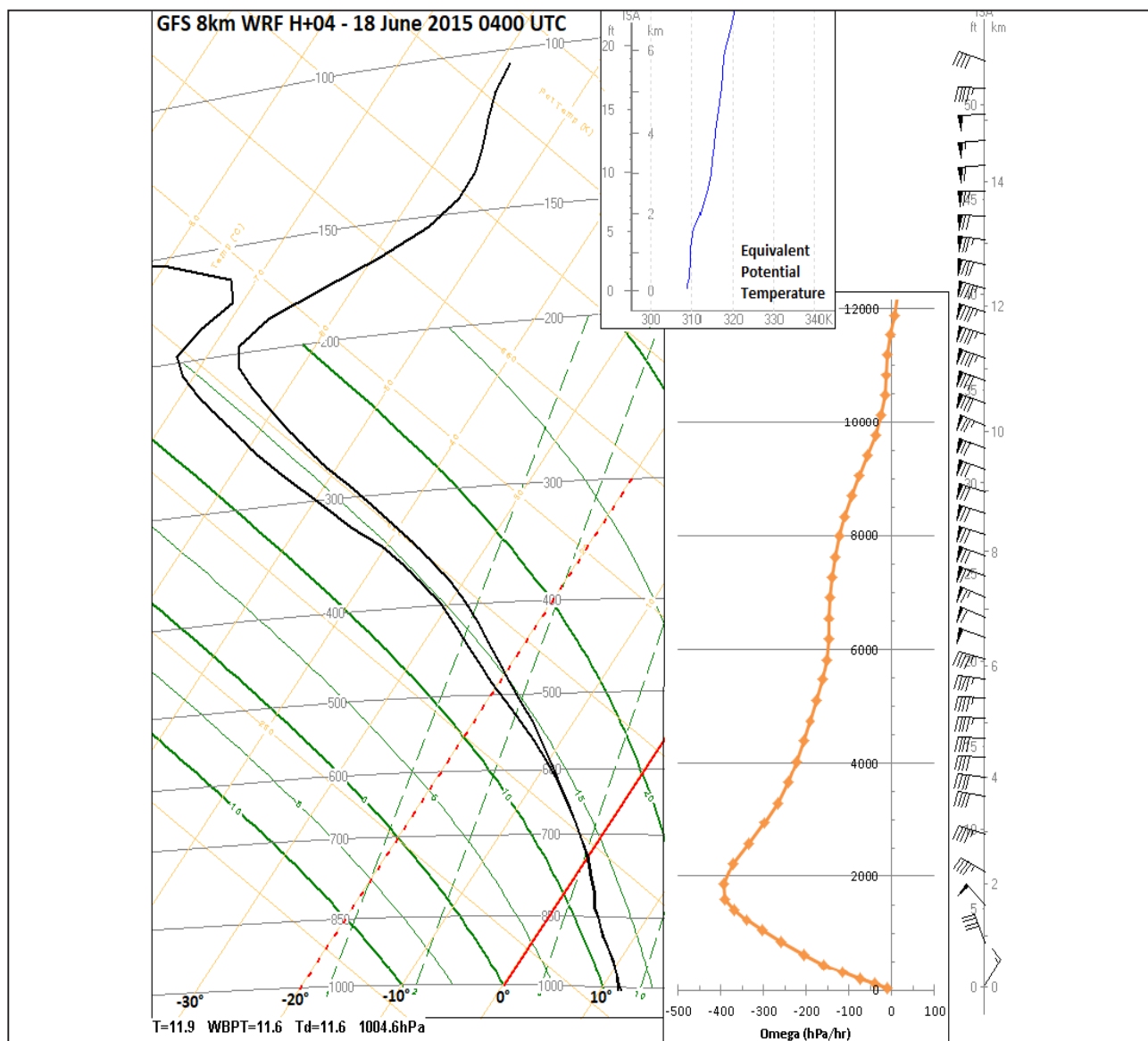


**Figure 6:** Model tephigram and vertical profiles for Hokitika Airport at 4pm (04:00 UTC) 18 June 2015 derived from the MetService 8km WRF model initialised off the 18/0000 UTC US NCEP/GFS global model. Orange lines orientated from top-right to bottom-left are isotherms; orange lines from top-left to bottom-right are dry adiabats; solid dark-green curves are saturated adiabats. The Equivalent Potential Temperature graph increases with height indicating a deep stable airmass. Vertical motion (omega) up to 12 km high is also shown and peaks around 2 km high. Wind barbs are in knots.

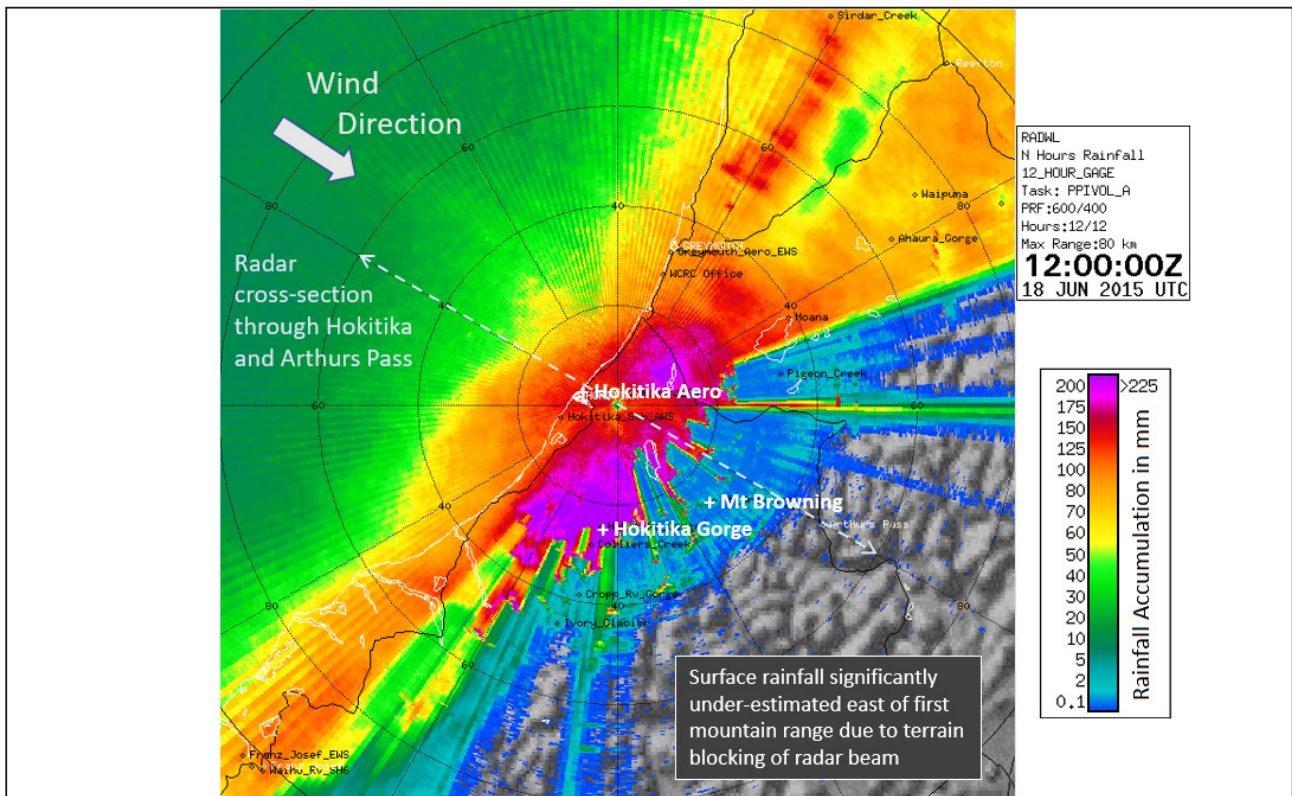


**Figure 7:** Gauge corrected radar rainfall accumulation from the MetService Westland radar for the 12-hour period from 00:00 UTC (Midday NZST) to 12:00 UTC (Midnight NZST) 18 June 2015. Radar reflectivity from the lowest clutter-free bin is used, using a Vertical Profile of Reflectivity correction to obtain the reflectivity at a fixed reference height of 0.1 km. Locations of the three rain-gauges in figure 8 are shown, as is the transect of the radar cross-section shown in figures 9, 10, 12 and 13.

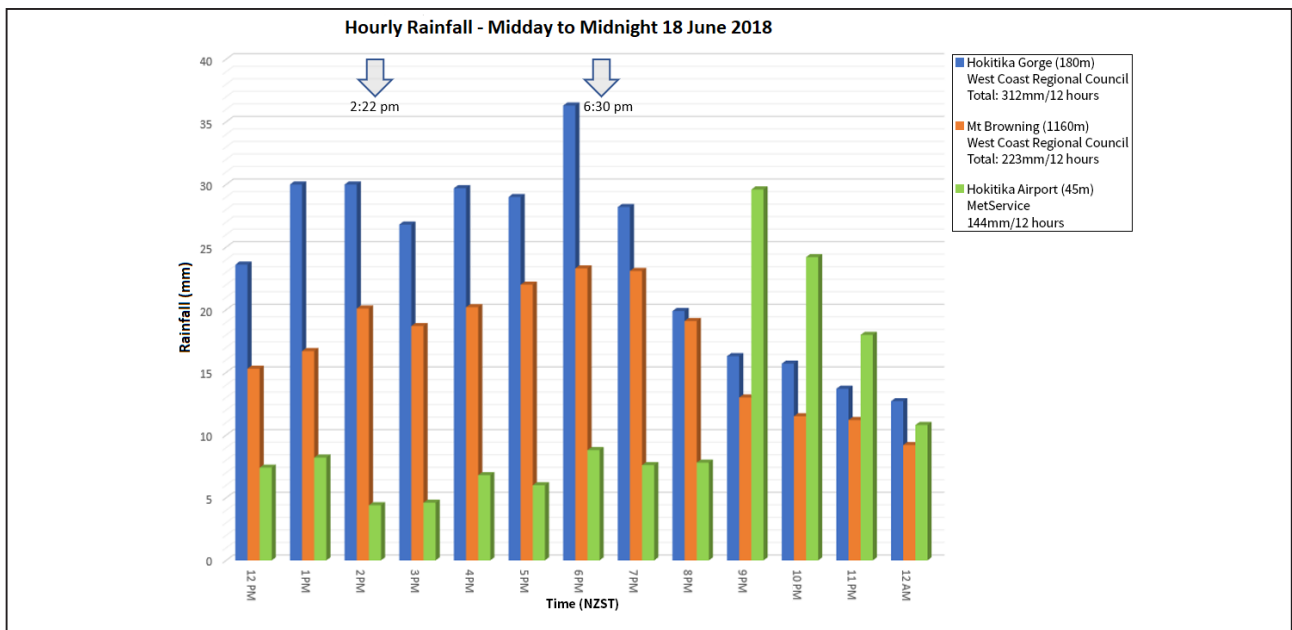


**Figure 8:** Hourly rainfall data for three gauges near the MetService Westland radar for the 12-hour period from midday to midnight NZST (00:00 to 12:00 UTC) 18 June 2015. The locations of the gauges are shown in figures 1 and 7. Hokitika Airport is near the coast, Hokitika Gorge is about midway between the coast and the main divide of the Southern Alps, and Mt Browning is an alpine station close to the main divide. The owner of the station and its height above sea level are included in the key. The times of the two radar vertical cross-sections discussed in section 4 are shown. The heavy rain recorded at Hokitika Airport around 9pm was associated with a shallow easterly wind change and is not discussed in this study.

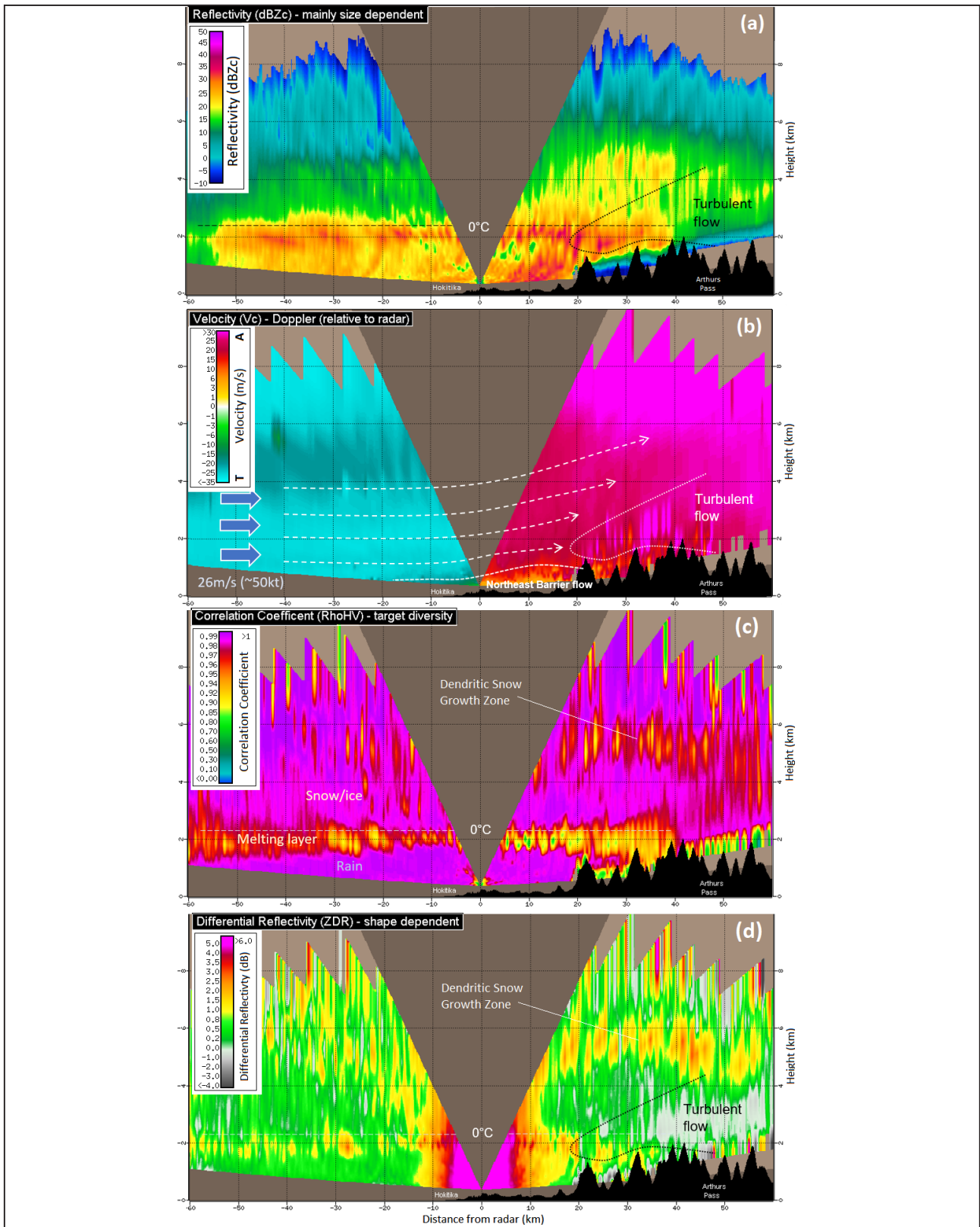


**Figure 9:** Westland radar vertical cross-sections at 02:22 UTC (2:22pm NZST) 18 June 2015. The 4 radar fields are (a) Horizontal Reflectivity (dBZ) corrected for attenuation, (b) Unfolded Doppler Radial Velocity (m/s), (c) Correlation Coefficient (unit-less), and (d) Differential Reflectivity (dB). The transect of the cross-section is shown in figure 7. The 0°C height is estimated from a combination of the radar imagery and the tephigram shown in figure 6.

#### 4.1. Radar Cross Sections at 02:22 UTC 18 June 2015

During the afternoon of 18 June 2015, rainfall rates of 25-30mm/h were recorded at Hokitika Gorge, while around 20mm/h was recorded at Mt Browning. Figure 9 shows a combined radar vertical cross-section at 02:22 UTC (2:22pm NZST) which is representative of the rainfall during this period. The cross-section shows four radar fields, (a) the horizontal Reflectivity ( $Z_H$ ) corrected for attenuation, (b) the unfolded Doppler Radial Velocity ( $V_C$ ), (c) the Correlation Coefficient ( $\rho_{HV}$ ) and (d) the Differential Reflectivity ( $Z_{DR}$ ) fields. The imagery shows stratiform precipitation only with no embedded convection. The estimated height of 0°C is marked on the imagery.

The melting layer shows as a band of enhanced reflectivities (~30 dBZ) known as the radar bright-band (Rinehart, 2010) just below 0°C in the reflectivity image (Figure 9a), but is better defined in the Correlation Coefficient field (Figure 9c) as a layer of reduced  $\rho_{HV}$  values (~0.75 to 0.95) and in the Differential Reflectivity field (Figure 9d) as a zone of enhanced  $Z_{DR}$  values (~1.0 to 3.0 dB). The melting layer is the region where falling ice crystals and snowflakes melt to raindrops. As the snowflakes melt, they first acquire meltwater on the outer portions of the flakes which leads to an increase in reflectivity ( $Z_H$ ). After further melting, the snowflakes collapse and become more oblate in shape before breaking up into individual and less oblate raindrops. It is this increasing oblateness during the melting process which produces the zone of larger positive Differential Reflectivity values (Kumjian, 2013). Also, as they melt, there is a mix of ice and snow, melting ice and snow, and fully melted raindrops within the melting layer which produces the zone of reduced Correlation Coefficient values (Kumjian, 2013). This mix of radar targets is greatest in the lowest half of the melting layer, which shows as reduced values of Correlation Coefficient ( $\rho_{HV}$  ~0.75 to 0.85) in Figure 9c. Note that the depth of the melting layer generally

appears to increase with distance from the radar in the Correlation Coefficient field, but this is due to the radar beams increasing in width at greater range and passing through the melting layer at a shallower angle which gives the incorrect appearance of a deeper melting layer further from the radar. Despite this, there is some evidence in both the Correlation Coefficient and Differential Reflectivity cross-sections of a deeper melting layer east of the radar under the stronger reflectivity echoes aloft which will be mainly due to downward penetration of snow in heavier precipitation, but also an above-mountain turbulent layer, as seen in Figure 9b and discussed later in this section, which may be throwing partially melted snow and ice crystals a little above the general melting level. The Correlation Coefficient image (Figure 9c) shows the melting layer depth to be about 500 metres west of the radar, and about 1km (or more) east of the radar in the heavier precipitation over the mountains. There are also lower  $\rho_{HV}$  values within the melting layer east of the radar indicating more target diversity and possibly larger aggregated snowflakes taking longer to melt and falling to a lower height (Kumjian, 2013).

The next zone which is easily observable is the Dendritic Snow Growth Zone (DGZ) at about 5-6km high. The DGZ is the region where the growth of dendritic snow crystals occurs and maximises between about -13°C and -17°C (Stoelinga et al., 2013). This generally occurs in regions of strong upward motion. The DGZ is characterised in the Correlation Coefficient field as a zone of reduced  $\rho_{HV}$  values (~0.90 to 0.98), and in the Differential Reflectivity field as a zone of increased positive values of  $Z_{DR}$  (~1.0 to 3.5 dB). These signatures are due to the rapid growth by deposition of planar or dendritic snow crystals within the zone (Kennedy and Rutledge 2011, Andric et al. 2013, Kumjian 2013). Within and below the DGZ, reflectivity ( $Z_H$ ) generally increases rapidly as the snow crystals fall out and aggregate into larger snowflakes (Kumjian 2013). Previous studies (Kennedy and Rutledge 2011, Bechini et al. 2013) have noted that these dual-polarisation radar

signatures observed around  $-15^{\circ}\text{C}$  (i.e. reduced  $\rho_{\text{HV}}$  and enhanced  $Z_{\text{DR}}$ ) correlate well with increased reflectivity, and precipitation rates, at the surface.

In the cross-sections (Figures 9c and 9d), the Dendritic Snow Growth Zone (DGZ) is particularly enhanced east of the radar over the mountains where the vertical motion is likely to be strongest (due to orographic lifting) compared to weaker signals over the sea west of the radar where vertical motion will be much weaker. These strong DGZ signatures aloft correlate well with increased reflectivity at lower levels, and the rapid increase in reflectivity within and immediately below the DGZ will be associated with aggregating snow crystals (Kumjian 2013). This all indicates that the growth of dendritic snow crystals is much stronger over the mountains and is likely to be one important mechanism in producing heavy precipitation at the surface. Interestingly, there is still a good Dendritic Snow Growth Zone signature east of the main divide (near Arthurs Pass village), although it does appear to lower in height. This suggests that significant numbers of dendritic snow crystals are still being produced aloft just east of the main divide and contributing to the production of “spill-over” precipitation by drifting downwind and falling farther east.

The radial velocity image (Figure 9b) is an unfolded Doppler wind field, and the cross-section is aligned with the prevailing northwest flow. Winds are shown relative to the radar with winds towards the radar on the left (negative values) and away from the radar on the right (positive values). Upwind of the radar (over the Tasman Sea), the northwest winds are strong and appear fairly uniform below about 4km, however the radar derived vertical wind profile in Figure 5a shows a wind speed maximum of about 50 knots (26m/s) over the radar at 2.5km amsl with slightly decreasing speed immediately above. The imagery also shows a low-level northeast barrier flow (indicated by reduced Doppler radial wind values due to the cross-wind component of the barrier flow) extending up to about 1.5km high and extending

over the coastal hills up to the first range of mountains about 20km east of the radar. There is also evidence of the barrier flow west of the radar but at a shallower height which dips below the radar beam offshore. It is interesting to note that the depth of the barrier flow does appear to be about twice as deep over the land east of the radar as it is near the coast.

Figure 10 shows a comparison between the raw radial velocity and the unfolded radial velocity cross-sections, taken along the same transect as Figure 9b. Although the strong northwest flow aloft is folded in the raw radial velocity cross-section (Figure 10a), and hence the towards/away winds are incorrect, the northeast barrier flow is depicted correctly and shows up well as a shallow layer below about 1km west and 1.5km east of the radar. Also evident in Figure 10a is a shallow turbulent layer along the top of the barrier flow which will be due to wind shear between the northeasterly winds in the barrier flow and the stronger onshore northwesterlies aloft.

More significantly, the Doppler radial velocity imagery (Figures 9b and 10a/b) shows a regularly-spaced variation in the velocity field immediately above the mountains to a depth of about 1-2km, which is similar to observations made by Houze and Medina (2005) over the European Alps (see also Rotunno and Houze, 2007). This is considered to be a turbulent flow generated by mechanical turbulence over the ranges. Note however, that in the unfolded velocity imagery (Figures 9b and 10b) the stronger “away” velocities showing within this turbulent flow are probably being incorrectly unfolded by the Vaisala IRIS software, and it may be depicted better in the raw radial velocity cross-section (Figure 10a). This is due to the software basing the unfolding on the vertical wind profile at the radar, which is all northwesterly, and assuming the same relative wind direction elsewhere. To explain the likely reason for this turbulence, consider the tephigram in Figure 6 which shows a deeply stable atmosphere, and the radar derived wind profile at 2:22pm in Figure 5a which shows a wind maximum of

---

about 26m/s (50kt) at 2.5km height above the radar and slightly decreasing wind speed above. Combined with the observed depth of the turbulent layer and the regular pattern in the Doppler Radial Velocity image (Figures 9b and 10), this suggests that the vertical shear associated with the observed wind maximum in Figure 5a is creating standing gravity waves over the mountains and these are likely to be trapped mountain waves (COMET, 2016). These trapped mountain waves, as observed at 02:22 UTC (Figures 9b and 10), are initially produced by the first range of mountains, then become complex over successive ranges, and increase in height over the higher terrain up to the main divide. Above this turbulent trapped mountain wave layer, the northwest flow appears

more laminar. The imagery also shows that the onshore northwest winds are lifted initially over the coastal barrier flow, confirming early modelling on barrier jets done by Revell et al. (2001) using 1996 SALPEX data, then appear to be lifted further over the mountain induced turbulent flow. This suggests the trapped mountain waves may be providing extra lift to the onshore winds and increasing the vertical motion upwind of the higher terrain.

The horizontal extent of the turbulent layers, as observed by the radar, is shown in Figure 11 which shows both the 2.0 degree raw (folded) and unfolded Doppler radial velocity PPI (Plan Position Indicator) imagery at 02:24 UTC. This 2.0 degree radar beam passes approximately

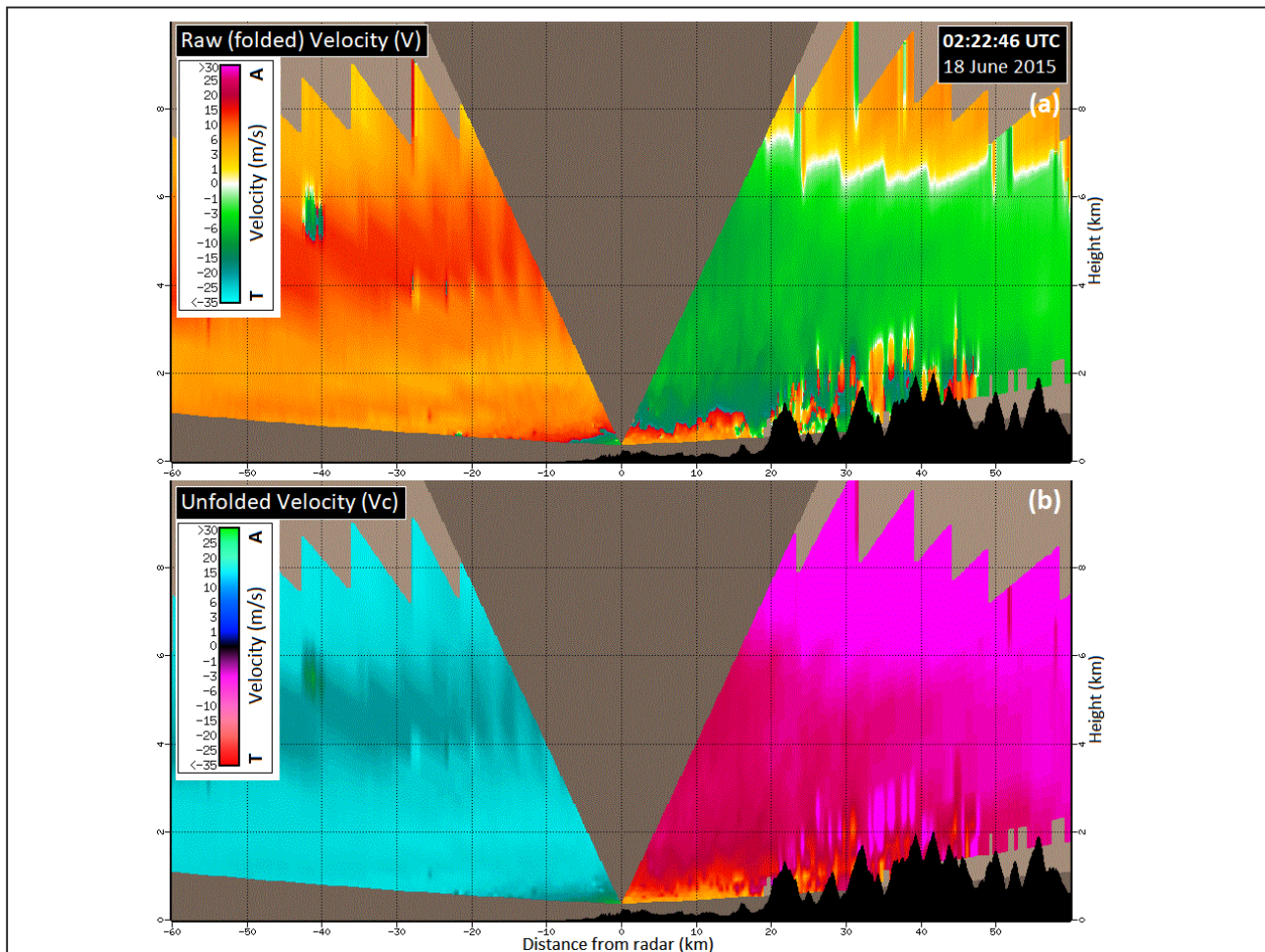


**Figure 10:** Vertical cross-sections showing the corresponding (a) raw and (b) unfolded Doppler Radial Velocity fields for the same time (02:22 18 June 2015 UTC), and along the same transect, shown in figure 9. The velocity data is unfolded using Vaisala IRIS software. Due to the strong northwest flow aloft, and a radar Nyquist Velocity of 16m/s, most of the data above the low-level northeast barrier in the raw velocity field is folded, and then corrected in the unfolded velocity field. Data within the turbulent layer over the mountains, however, is probably incorrectly unfolded by the software due to the complicated nature of the turbulence. On the scale bar, T indicates “towards radar” velocities, and A indicates “away from radar” velocities.

along the top of the barrier flow east of the radar and through the centre of the turbulent layer over the mountains. A shear turbulent layer, generated by vertical wind shear between the northeast barrier flow and the stronger onshore northwest flow aloft, shows in both images as a set of approximately parallel lines just east of the radar. Immediately downwind of this, the mechanical turbulent layer over the mountains shows as a broad zone of mixed towards and away velocities in the raw velocity field (Figure 11a) and as a broad zone of strong variable away velocities in the unfolded velocity field (Figure 11b). As mentioned above however, the velocities within this zone are probably being unfolded incorrectly by the software. The mechanical turbulent layer appears very noisy in the PPI imagery due to the complex nature of the turbulence and the underlying terrain but does show a more wave-like structure in the vertical radial velocity cross-sections (Figure 10) discussed earlier. This mechanical turbulent layer was observed on both the PPI and cross-section imagery to be persistent though the whole period of heavy rain during the afternoon and

evening of 18 June 2015. It consistently extended over the main divide towards Arthurs Pass village, but at times did vary in intensity and often extended well east of the main divide of the Southern Alps. Note however, that at 02:24 UTC (Figure 11), it is possible the 2.0 degree radar beam may be overshooting any lower waves east of Arthurs Pass due to the increasing height of the beam with range, and lower elevation beams from the Hokitika radar are unable to detect them due to terrain blocking.

The reflectivity image (Figure 9a) shows an increase in reflectivity below the melting layer and within the barrier flow (about 10-20km east of the radar) which results in enhanced surface rainfall. This enhancement is likely the result of a collectional growth (or seeder-feeder) type mechanism where falling precipitation collides and coalesces with smaller cloud droplets within the moist barrier flow (Houze, 2012, Stoelinga et al., 2013). Stoelinga et al. (2013) notes this often occurs in cases with a high melting layer, and Figures 9a/c/d show the melting layer to be around 2-3km high in this area. A similar

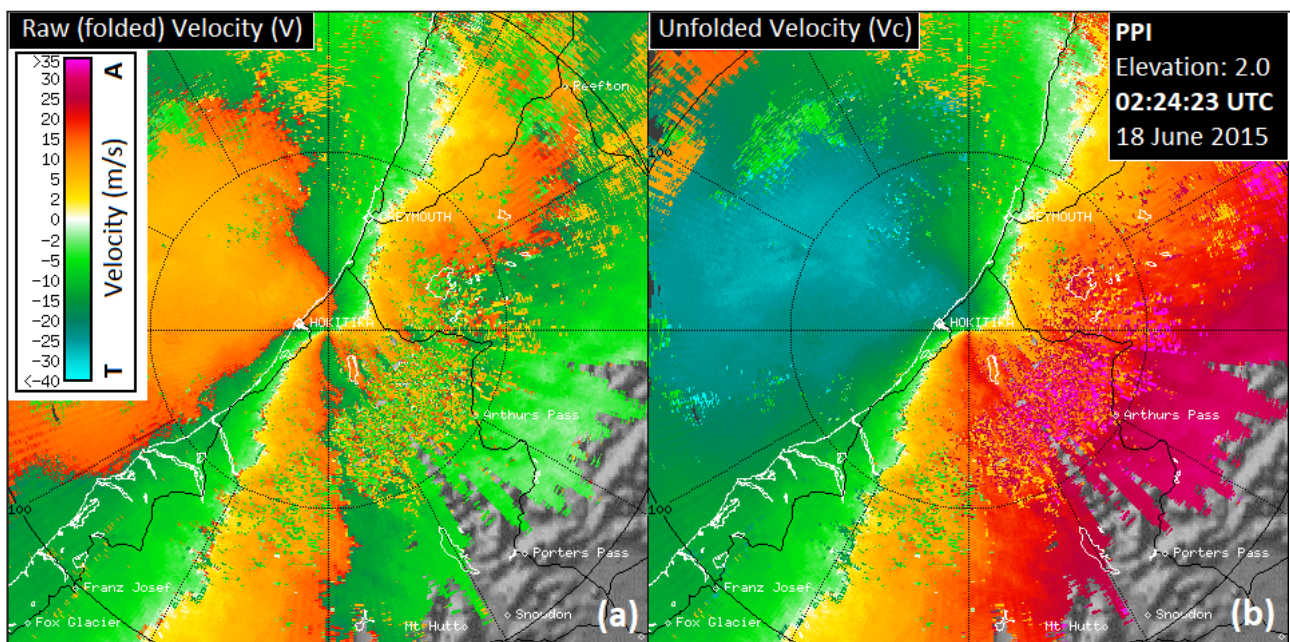


**Figure 11:** 2.0 degree Plan Position Indicator (PPI) images showing (a) raw Doppler Radial Velocity and (b) unfolded Doppler Radial Velocity at 02:24 18 June 2015 UTC. The velocity field is unfolded using Vaisala IRIS software. Most of the data is considered to be correctly unfolded by the software, however the data within the broad turbulent zone observed over the mountains is probably incorrectly unfolded due to the complicated nature of the turbulence. On the scale bar, T indicates “towards radar” velocities, and A indicates “away from radar” velocities. Range rings are shown at 50km and 100km from the radar.

seeder-feeder enhancement was observed by Purdy et al. (2005) with X-band radars on the South Island West Coast during the 1996 SALPEX experiment (Wratt et al, 1996), however their study involved a more classical seeder-feeder type event where snow falling from a separate system aloft fell into a lower shallow raining cloud system.

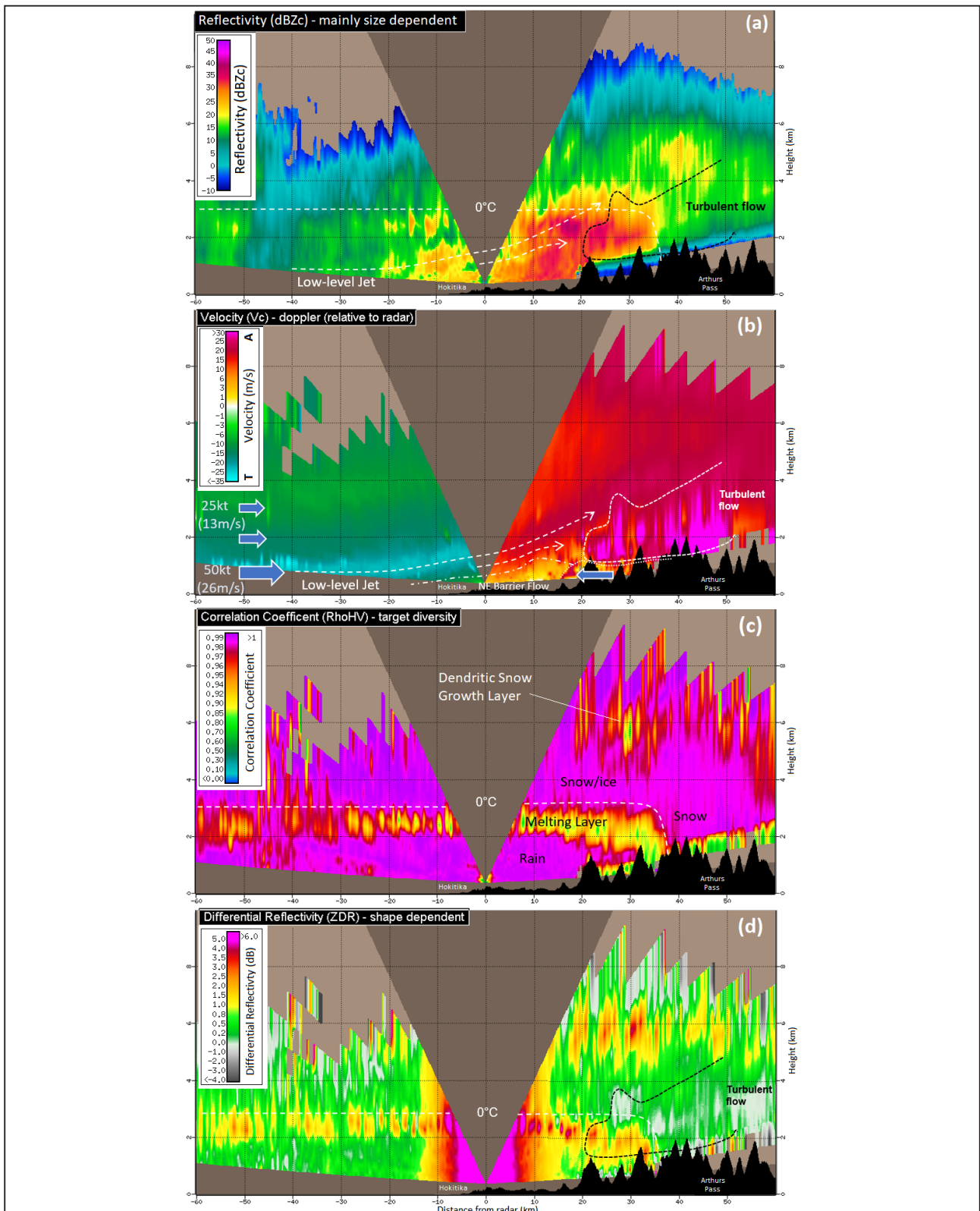
#### 4.2. Radar Cross Sections at 06:30 UTC 18 June 2015

Figure 12 shows the same radar cross-sections as in Figure 9 but at 06:30 UTC, while Figure 13 shows in more detail the raw and unfolded radial Doppler velocity cross-sections. The imagery in Figure 12 again clearly shows the melting layer at 2-3km high and the Dendritic Snow Growth Zone (DGZ) around 5-7km high over the mountains, but it also shows several significant changes from the previous time, most of which can be attributed to changes in the structure of the onshore northwesterly flow. In the Doppler radial velocity imagery, the previous cross-sections at 02:22 UTC (Figures 9b and 10a/b) and the associated wind profile in Figure 5a showed a slight wind speed maximum about 2.5km high, but at 06:30 UTC (Figures 12b and 13a/b), this has now changed to a better-defined low-level jet of around 50kt (26m/s), centred about 1km high over the sea west of the radar. The northeast barrier flow is still well marked up to about 1.5km height east of the radar up to near the first range of mountains, and there is still a strong trapped mountain wave turbulent layer downstream of the first range of mountains which increases in height from about 2km high to about 4km high over the area just east of the main divide above Arthurs Pass village. This mountain wave turbulent signature appears to be stronger and better defined than at 02:22 UTC. The low-level jet can also be observed being lifted to higher elevations above the barrier flow and over the mountains. This is presumably transporting significant amounts of low-level moisture up into the riming and aggregation zones, and may also be creating a stronger mountain wave turbulent layer due

to the greater vertical wind shear and reduction in cross-barrier flow above the ascending jet (COMET, 2016). Also observable on the Doppler radial velocity images (Figures 12b and 13) is a shallow cold easterly flow (marked by the right arrow in Figure 12b) which has moved across the Southern Alps main divide from Canterbury. Note however, that due to incorrect assumptions made by the velocity unfolding software, this easterly wind in the unfolded imagery (Figures 12b and 13b) is shown as a positive “away” wind rather than a negative “towards” wind.

In Figure 12, both the melting layer and Dendritic Snow Growth Zone (DGZ) are about 500 m higher than at 02:22Z indicating a warming of the airmass. The Correlation Coefficient and Differential Reflectivity imagery (Figures 12c and 12d) also show a sharp lowering of the melting layer over the mountains about 35km east of the radar associated with the much colder easterly flow advecting across the Southern Alps from Canterbury where snow was falling to low levels over the Canterbury Plains. This is a good example of a warm advection snowfall event where a shallow layer of much colder denser air is undercutting a deep warm moist layer aloft (Neale and Thompson, 1977, MetService, 2015).

The strongest DGZ and reflectivity signatures aloft in Figure 12 are generally further east than at 02:22 UTC, however there is still a good DGZ signature showing in both the Correlation Coefficient and Differential Reflectivity images (Figures 12c and 12d) above, and slightly upwind of, the first range of mountains. The area of enhanced reflectivity (20-25 dBZ) between about 4 and 6 km high (30 to 50 km east of the radar) will be associated with aggregating snowflakes, while the lower area of enhanced reflectivities (20-30 dBZ) between 3 and 4 km high (and extending out to about 35 km east of the radar) will be due to riming and aggregation (Andric, et al., 2013). This lower enhanced reflectivity area lies within the ascending low-level jet, and near the top of the



**Figure 12:** Westland radar vertical cross-sections at 06:30 UTC (6:30pm NZST) 18 June 2015. The four radar fields are (a) Horizontal Reflectivity (dBZ) corrected for attenuation, (b) Unfolded Doppler Radial Velocity (m/s), (c) Correlation Coefficient (unit-less), and (d) Differential Reflectivity (dB). The transect of the cross-section is shown in Figure 7. The 0°C height is estimated from a combination of the radar imagery and the model tephigram shown in Figure 6.

turbulent layer, and it is likely that there are significant amounts of super-cooled liquid water in this region causing strong riming (Grazioli, 2015).

Below the melting layer, in the area about 10-20 km east of the radar, there is a deep layer of enhanced reflectivities (30-40dBZ, Figure 12a) extending from the melting layer to the surface that will be associated with very heavy rain. This is the heavy rain that affected the Hokitika Gorge rain gauge around this time when rainfall rates in excess of 30 mm/h were recorded (Figure 8). This region of observed heavy rain lies within both the warm part of the ascending low-level jet and the northeast barrier flow suggesting the enhancement is due to a strong collision-coalescence and/or collectional growth (or seeder-feeder) type affect as falling precipitation generated aloft collides with smaller cloud or drizzle droplets advected into this area below the melting layer.

## 5. 6.0° PPI Radar Imagery – 06:30 UTC 18 June 2015

To get a better understanding of the microphysical processes producing the heavy orographic rain, we can look at an individual radar beam that slices through the all the zones identified in the cross-sections discussed in section 4. Figure 14 shows the position of the 6.0° beam on the 06:30 UTC cross-section discussed in section 4.2. The radar beam lies near the path of the ascending low-level jet below the melting layer, then lies near the top, or just above, the embedded mountain wave turbulent layer at higher elevations. Figure 15 shows the 6.0° PPI (Plan Position Indicator) imagery for four radar fields at 06:30Z. In this type of imagery, layers of constant elevation show as circular rings.

In Figure 15, the melting layer is well defined just below

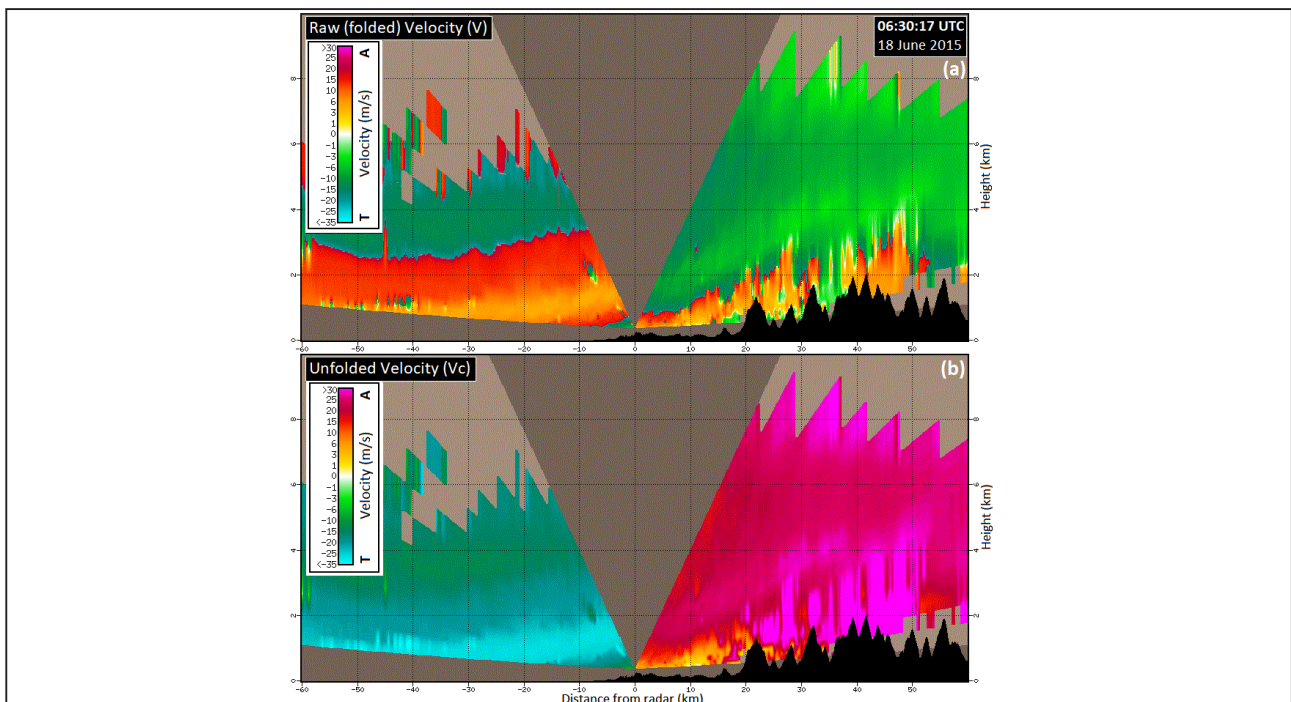


**Figure 13:** Vertical cross-sections showing the corresponding raw (top) and unfolded (bottom) Doppler Radial Velocity fields for the same time (06:30 18 June 2015 UTC), and along the same transect, shown in figure 12. The velocity data is unfolded using Vaisala IRIS software. Due to the strong north-west flow aloft, and a radar Nyquist Velocity of 16m/s, much of the data above the low-level northeast barrier in the raw velocity field is folded, and then corrected in the unfolded velocity field. A shallow easterly wind change moving through the mountains east of the radar has been incorrectly unfolded by the software and is shown correctly in the raw velocity image. Data within the turbulent layer over the mountains is also probably incorrectly unfolded by the software due to the complicated nature of the turbulence. On the scale bar, T indicates “towards radar” velocities, and A indicates “away from radar” velocities.

0°C as a ring of enhanced reflectivities of around 30 to 40 dBZ (the radar bright band) on the reflectivity image (Figure 15a), a ring of reduced values of around 0.75 to 0.95 in the Correlation Coefficient image (Figure 15b), and a ring of enhanced positive Differential Reflectivity values of around 1.0 to 3.0 dB (Figure 15c). The other area of very high Differential Reflectivities below the melting layer and near the radar is noise from an unknown systematic bias. Similarly, on the Specific Differential Phase image (Figure 15d) the large area of negative KDP values near the radar is also considered to be noise from an unknown systematic bias and is masking any melting layer signals.

The Dendritic Snow Growth Zone (DGZ) is well defined in the zone between -10° and -20°C over the land (likely maximising around -13° to -17°C, Stoelinga et al., 2013), and is particularly strong over the mountains east of the radar due to the strong vertical motion from orographic lifting and moisture transported into this region by the ascending onshore flow (as discussed in section 4.2). The DGZ is observed as an outer ring of reduced Correlation Coefficient values ( $\rho_{HV} \sim 0.95$ ), and enhanced positive

values of both Differential Reflectivity ( $Z_{DR} \sim 1.0$  to 3.0 dB) and Specific Differential Phase ( $K_{DP} \sim 1.0$  to 2.0 deg/km). The  $\rho_{HV}$ ,  $Z_{DR}$  and  $K_{DP}$  rings are co-located, and the maximum values of the outer  $K_{DP}$  ring generally lies just below the  $Z_{DR}$  maximum. Reflectivity ( $Z_H$ ) increases from about the middle of the DGZ towards the ground suggesting the aggregation of dendritic snow crystals in the lower part of the Dendritic Snow Growth Zone. These observations are consistent with the findings of others (e.g. Andric 2013, Schrom 2015). Interestingly, the DGZ does not appear to be perfectly circular which indicates its height varies. This is likely related to changes in the strength of the vertical motion due to terrain effects which may be altering the temperature structure within the cloud system over the mountains.

Of significant interest is a third zone of strongly enhanced KDP values showing between about -5°C and -10°C on the Specific Differential Phase image (Figure 15d). This zone is associated with a slight enhancement of  $Z_{DR}$  values and a slight reduction in  $\rho_{HV}$  values. There is also a decrease in reflectivity  $Z_H$  values within this zone, but they do increase again immediately below it. This

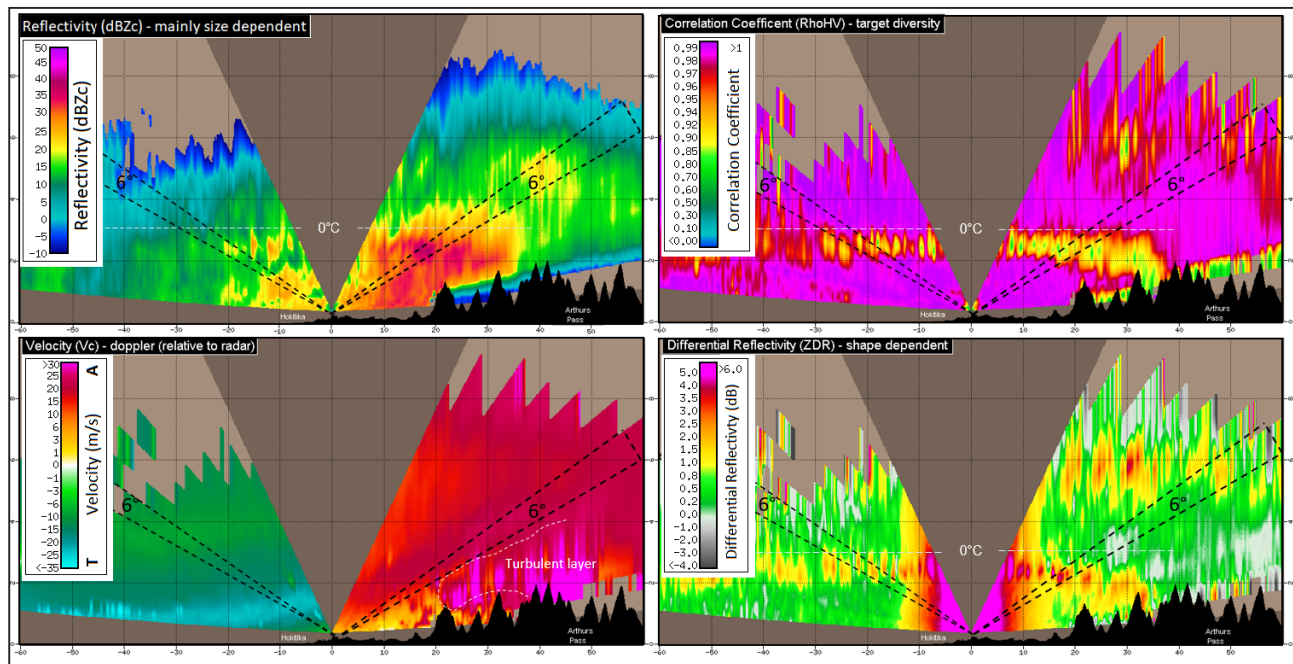


**Figure 14:** Westland radar vertical cross sections for 06:30 UTC 18 June 2015 (same as figure 12) showing the position of the 6.0° radar beam used for the PPI imagery in figure 15.

zone also appears to lie just above the turbulent layer observed in Figures 9 and 12. This signature is not well documented in the literature but was very persistent for this event and is often observed on the Westland radar over the mountains during heavy orographic rainfall events. The reduction of  $Z_H$  values suggest that the snow/ice aggregates are reducing in size within this zone, and the strong  $K_{DP}$  signature combined with only a minor increase in  $Z_{DR}$  values suggests there may be a significant increase in the target density in this area. It is therefore possible that this may be an ice-splintering and riming zone, possibly due to the turbulent layer below. If there is a significant increase in the number of targets/ice particles

within this zone, and these can then grow further through riming and/or coalescence at lower levels, then this will significantly increase precipitation rates at the surface.

### 6. The role of turbulence in enhancing orographic precipitation

The radar imagery (Figures 9, 10, 11, 12 and 13) shows a significant and persistent trapped mountain-wave turbulent layer extending 1-2 km above the mountains up to and often beyond the main divide of the Southern Alps. This raises the question of whether or not this turbulent layer plays any contributing role in the production of

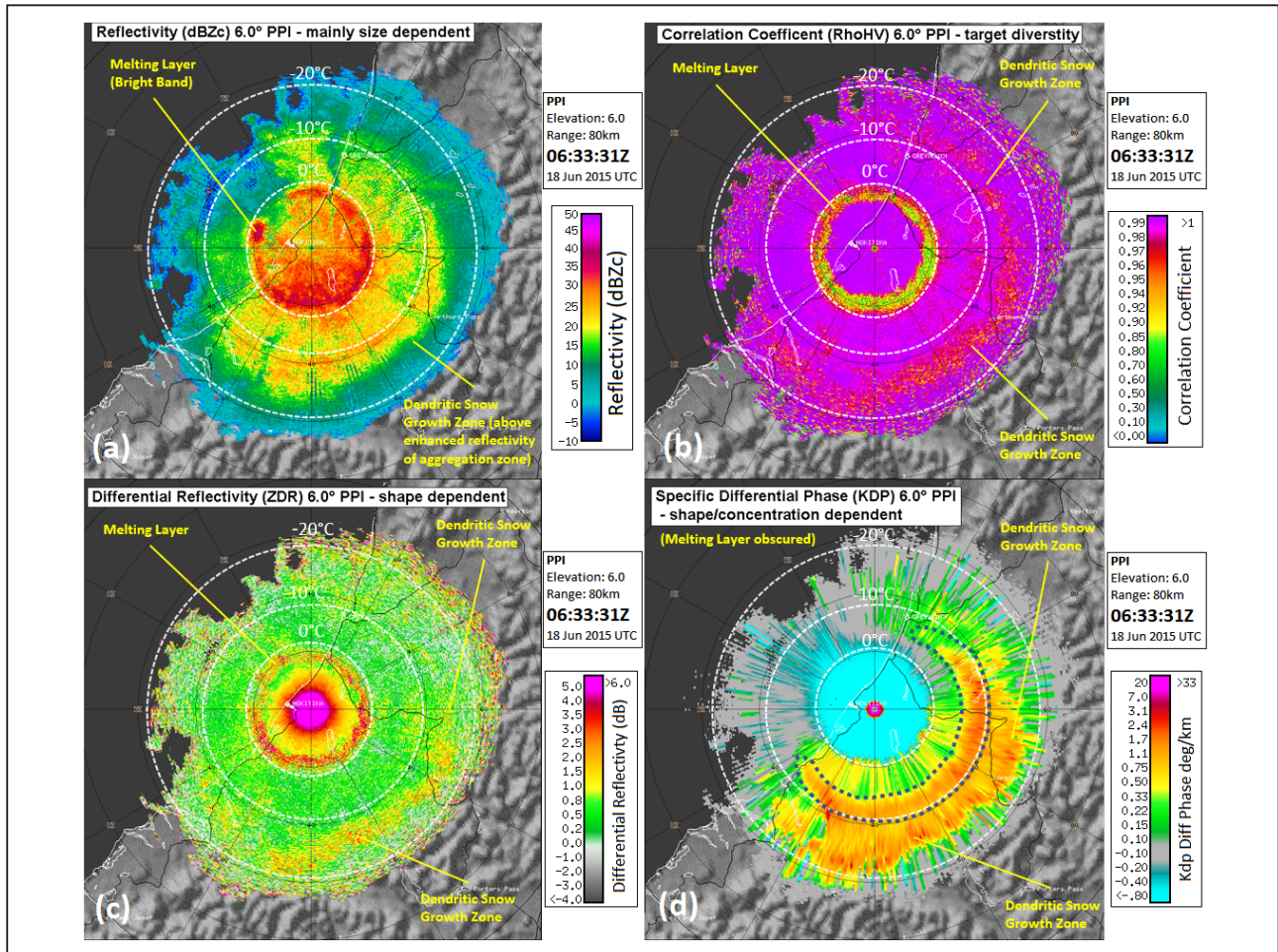


**Figure 15:** 6.0° Westland radar PPI (Plan Position Indicator) images for 06:30 UTC (6:30pm NZST) 18 June 2015. The 4 radar fields are (a) Horizontal Reflectivity (dBZ) corrected for attenuation, (b) Correlation Coefficient (unit-less), (c) Differential Reflectivity (dB), and (d) Specific Differential Phase (deg/km). The melting layer and Dendritic Snow Growth Zones are marked, as are approximate temperatures for 0°C, -10°C and -20°C (derived from the Hokitika Airport model tephigram shown in figure 6). Also marked on the Specific Differential Phase image is a secondary intermediate zone lying between the melting layer and the Dendritic Snow Growth Zone at approximately -5° to -10°C.

heavy rain at the surface. The Doppler radial velocity cross-sections in Figures 9b and 12b (also Figures 10 and 13) clearly show the onshore northwest flow being lifted above the turbulent layer so it does appear to provide extra lift to the ascending low-level moisture, but is it also enhancing the production of precipitation particles aloft?

Several studies have shown that turbulence does play an important role in enhancing snow crystal growth aloft (e.g. Houze and Medina, 2005, Geerts et al, 2011, Grazioli et al, 2015, Aikins et al. 2016). This turbulence can be the result of vertical wind shear (e.g., the layer between the lower blocked barrier flow and the unblocked flow above), or from orographically induced eddies/oscillations triggered by the flow of stable air over rough terrain/ridgelines (e.g., the trapped mountain waves observed in Figures 9b, 10, 12b and 13). Turbulent updrafts embedded within the flow, such as those associated with the trapped mountain waves observed in Figures 9b, 10, 12b and 13, can create pockets of highly concentrated super-cooled liquid water embedded within an orographic cloud sheet which leads to increased riming of dendritic snow-flakes/crystals falling from above (Houze and Medina 2005, Stoelinga et al. 2013). Houze and Medina (2005) found this produced heavier, more rapidly falling precipitation particles which have a higher probability of reaching the ground upwind of a mountain crest, and that without the turbulent cells, condensate would more likely be advected farther up and perhaps even over the mountain range. The observed trapped mountain waves embedded within the flow (Figures 9b, 10, 12b and 13) may also provide a favourable regime allowing heavier rimed snow crystals to fall more directly to the ground within downdrafts, and also promote further growth of ice crystals through aggregation by creating a field of highly variable and turbulent air motions which makes it easier for ice crystals to collide and stick together. At lower levels, turbulence within the warm cloud layer (i.e., temperature warmer than 0°C) also enhances coalescence through more collisions (Houze and Medina, 2005, Geerts et al., 2011).

Grazioli et al, (2015) provide a possible explanation for the observed intermediary  $K_{DP}$  layer observed in Figure 15d and relate this to turbulence. Although they mainly considered small-scale turbulence, the ideas may still be applicable to the deeper turbulent layer observed in this study. They suggest that wind shear and updrafts within the turbulent layer together continuously feed the regions above the shear layer with super-cooled liquid water and ice fragments, and favour the growth of anisotropic (directionally dependent, usually with a horizontal orientation) ice crystals at this level. This growth of anisotropic ice crystals creates an enhancement of  $Z_{DR}$  and  $K_{DP}$  in polarimetric radar imagery. Ice multiplication effects within the riming zone, and the availability of large quantities of small crystals fed from the turbulent layer below, both likely contribute to the stronger secondary peak of  $K_{DP}$  which is observed in Figure 15d between the more common higher level  $K_{DP}$  peak associated with dendritic snow growth aloft and a lower peak associated with the melting layer (which is hidden by noise from an unknown systematic bias close to the radar in Figure 15d). As mentioned previously, this observed secondary peak of  $K_{DP}$  is not well documented in the literature and doesn't appear at this strength and intensity in non-orographic or weaker orographic stratiform precipitation (whereas both the dendritic-zone and melting-layer peaks generally do).

## 7. Conclusion

The polarimetric radar imagery presented in this study has clearly shown several processes responsible for producing the observed heavy orographic rainfall. Some of these processes are confirmation of the existing knowledge related to South Island West Coast orographic rainfall, but some are new ideas to New Zealand.

Confirmation of existing knowledge:

- The radar imagery confirms the idea that the initial lifting of the low-level moisture occurs over the

northeast barrier flow (as modelled by Revell et al., 2002), then rises further over the mountains providing moisture to the snow-growth and riming zones.

- The polarimetric radar imagery clearly shows the melting layer and Dendritic Snow Growth Zone, which are both enhanced over the mountains. These layers are both well-known and documented features in polarimetric radar imagery and are observable in most deep stratiform rain systems (for further detail see Kumjian, 2013).
- The main microphysical growth mechanisms in the production of heavy orographic stratiform rainfall are the deposition processes (especially the growth of dendrites, which maximises around -13 to -17°C in the region known as the Dendritic Snow Growth Zone), and the accretion processes (i.e., riming (cold cloud), aggregation (cold cloud) and collision/coalescence (warm cloud)), with deposition, riming and collision/coalescence likely the most important (for further detail see Stoelinga et al., 2013).
- Ice multiplication/splintering is likely to be important in the production of heavy stratiform rain as it provides more ice crystals which can grow further through riming and aggregation (for further detail see Hallott and Mossop, 1974; Grazioli et al., 2015).
- The downwind drift of lighter snowflakes formed aloft on the western side of the Southern Alps leads to spillover precipitation east of the main divide (as suggested by Sinclair et al., 1997, Chater and Sturman, 1998)

The radar imagery also reveals some additional processes associated with heavy orographic rain on the South Island West Coast, which are consistent with the findings of previous studies (e.g. Houze et al.,

2005, Geerts et al., 2011, Grazioli et al., 2014, Aikins et al., 2016). Specifically, as discussed in section 6, the observed trapped mountain waves embedded within the rainband and associated turbulence are considered to be an important mechanism for the enhancement of the orographic precipitation by providing additional lift to the onshore airmass and enhancing ice crystal growth aloft. The radar cross sections (Figures 9 and 12) showed the low-level moisture being lifted quickly up into the snow and ice growth regions, with a strongly enhanced Dendritic Snow Growth Zone observed in the Correlation Coefficient and Differential Reflectivity imagery (Figures 9c/d and 12c/d) immediately above, and even slightly upwind, of the first range of mountains. This would have produced significant numbers of snow crystals well upwind of the highest terrain that grew further through aggregation and riming at lower levels due to the turbulent trapped mountain waves producing pockets of highly concentrated super-cooled liquid water. This, combined with a lighter horizontal wind regime and the associated updrafts and downdrafts within the embedded trapped mountain waves, would have produced heavier, more rapidly falling precipitation particles which had a higher probability of reaching the ground well upwind of the main divide. These processes are considered to have significantly contributed to producing the heavy stratiform rain observed over the mountains upwind of the main divide, and when combined with the strong collision-coalescence and/or collectional growth type effects observed at lower levels in section 4 (Figures 9 and 12), most likely increased the rainfall nearer the coast leading to the significantly heavier rain recorded at the Hokitika Gorge rain-gauge compared to the Mt Browning gauge which is located at a higher elevation farther downwind closer to the main divide (Figure 8).

A secondary (intermediate) ice-growth region was also observed in the Specific Differential Phase ( $K_{DP}$ ) imagery between the melting layer and the Dendritic Snow Growth Zone (Figure 15). This zone is not well documented in the

literature and is considered to be a riming and splintering (ice multiplication) zone which is not always as strong or as well defined in other non-orographic stratiform rain systems. This zone appears to be related to heavy surface precipitation, and possibly indicates large numbers of small, splintered ice crystals undergoing riming. As discussed in section 6, the combination of wind shear and vertical updrafts/downdrafts within the turbulent mountain wave layer may have broken up falling ice crystals and fed the regions above with small ice fragments that grew further through the riming process leading to more precipitation. It is suggested that the embedded mountain wave/turbulent layer and the intermediate enhanced  $K_{DP}$  layer observed in the radar imagery are related, and probably act together to enhance surface precipitation in mountainous terrain.

In conclusion, this study has shown that the dominant microphysical processes involved in producing the heavy orographic rain observed during this event are related to the strength and location of the dendritic snow growth zone, the riming and ice splintering above the mountain wave turbulent layer, and the enhancement of the rainfall at low levels by warm rain processes (i.e., collision-coalescence and collectional growth). The turbulent layer embedded within the rainband appears to be an important mechanism in enhancing the first two of these processes, and, when combined with warm rain effects at lower levels, may also be a factor in shifting the maximum rain accumulations well upwind of the Southern Alps main divide nearer to the first range of mountains. Due to their short horizontal wavelength, these mountain waves are generally poorly resolved by numerical weather prediction (NWP) models, and this may be one of the reasons the forecast models occasionally under-estimate the rainfall about the Southern Alps. Future work to improve the forecasting and modelling of these embedded turbulent mountain waves could lead to a better understanding of the observed rainfall distribution about the mountains on the South Island West Coast. Other future work could

include using the MetService Westland radar to scan above the mountains at a better vertical resolution and higher Nyquist velocity, and maybe even using a separate vertically-pointing Doppler radar located within the mountains west of the main divide, to better understand the above-mountain turbulent layer and its contribution to enhancing the surface rainfall.

## Acknowledgements

The authors would like to thank West Coast Regional Council and MetService for the use of their rain-gauge data, and MetService for the radar data used in this study.

## References

- Aikins, J., Friedrich, K., Geerts, B. and Pokharel, B., 2016. Role of a cross-barrier jet and turbulence on winter orographic snowfall. *Monthly Weather Review*, 144(9), pp.3277-3300.
- Andrić, J., Kumjian, M.R., Zrnić, D.S., Straka, J.M. and Melnikov, V.M., 2013. Polarimetric signatures above the melting layer in winter storms: An observational and modeling study. *Journal of Applied Meteorology and Climatology*, 52 (3), pp.682-700.
- Bechini, R., Baldini, L. and Chandrasekar, V., 2013. Polarimetric radar observations in the ice region of precipitating clouds at C-band and X-band radar frequencies. *Journal of Applied Meteorology and Climatology*, 52 (5), pp.1147-1169.
- Chater, A.M. and Sturman, A.P., 1998. Atmospheric conditions influencing the spillover of rainfall to lee of the Southern Alps, New Zealand. *International Journal of Climatology: A Journal of the Royal Meteorological Society*, 18 (1), pp.77-92.
- COMET, 2016. MetEd: Forecasting Mountain Wave Turbulence for Aviation, viewed 26 July 2021. University Corporation for Atmospheric Research. <[www.meted.ucar.edu/aviation/mtnwave\\_turbulence](http://www.meted.ucar.edu/aviation/mtnwave_turbulence)>
- Geerts, B., Miao, Q. and Yang, Y., 2011. Boundary layer turbulence and orographic precipitation growth in cold clouds:

- Evidence from profiling airborne radar data. *Journal of the atmospheric sciences*, 68(10), pp.2344-2365.
- Grazioli, J., Lloyd, G., Panziera, L., Hoyle, C.R., Connolly, P.J., Henneberger, J. and Berne, A., 2015. Polarimetric radar and in situ observations of riming and snowfall microphysics during CLACE 2014. *Atmospheric Chemistry and Physics*, 15 (23), pp.13787-13802.
- Hallett, J. and Mossop, S.C., 1974. Production of secondary ice particles during the riming process. *Nature*, 249 (5452), pp.26-28.
- Henderson, R.D. and Thompson, S.M., 1999. Extreme rainfalls in the southern Alps of New Zealand. *Journal of Hydrology (New Zealand)*, pp.309-330.
- Houze Jr, R.A., 2012. Orographic effects on precipitating clouds. *Reviews of Geophysics*, 50 (1).
- Houze Jr, R.A. and Medina, S., 2005. Turbulence as a mechanism for orographic precipitation enhancement. *Journal of the atmospheric sciences*, 62 (10), pp.3599-3623.
- Kennedy, P.C. and Rutledge, S.A., 2011. S-band dual-polarization radar observations of winter storms. *Journal of Applied Meteorology and Climatology*, 50 (4), pp.844-858.
- Kumjian, M.R., 2013. Principles and Applications of Dual-Polarization Weather Radar. Part II: Warm-and Cold-Season Applications. *Journal of Operational Meteorology*, 1.
- Macara, G.R., 2018. The climate and weather of New Zealand. NIWA Science and Technology Series 74, 50 pp.
- MetService 2015, Snowfall in New Zealand, MetService, viewed 26 July 2021, <<https://blog.metservice.com/node/1063>>
- Moisseev, D.N., Lautaportti, S., Tyynela, J. and Lim, S., 2015. Dual-polarization radar signatures in snowstorms: Role of snowflake aggregation. *Journal of Geophysical Research: Atmospheres*, 120 (24), pp.12644-12655.
- Neale, A.A. and Thompson, G.H., 1977. Meteorological conditions accompanying heavy snowfalls in southern New Zealand. New Zealand Meteorological Service.
- Purdy, J.C. and Austin, G.L., 2003. The role of synoptic cloud in orographic rainfall in the Southern Alps of New Zealand. *Meteorological Applications: A journal of forecasting, practical applications, training techniques and modelling*, 10(4), pp.355-365.
- Purdy, J.C., Austin G.L., Seed A.W., Cluckie I.D., 2005. Radar evidence of orographic enhancement due to the seeder feeder mechanism. *Meteorological Applications*, 12 (3), pp 199-206.
- Revell, M.J., Copeland, J.H., Larsen, H.R. and Wratt, D.S., 2002. Barrier jets around the Southern Alps of New Zealand and their potential to enhance alpine rainfall. *Atmospheric research*, 61 (4), pp.277-298.
- Rinehart, R.E., 2010. Radar for Meteorologists, Or, You Too Can be a Radar Meteorologist, Part III. Rinehart Publications.
- Rotunno, R. and Houze, R.A., 2007. Lessons on orographic precipitation from the Mesoscale Alpine Programme. *Quarterly Journal of the Royal Meteorological Society: A journal of the atmospheric sciences, applied meteorology and physical oceanography*, 133 (625), pp.811-830.
- Schrom, R.S., Kumjian, M.R. and Lu, Y., 2015. Polarimetric radar signatures of dendritic growth zones within Colorado winter storms. *Journal of Applied Meteorology and Climatology*, 54 (12), pp.2365-2388.
- Sinclair, M.R., Wratt, D.S., Henderson, R.D. and Gray, W.R., 1997. Factors affecting the distribution and spillover of precipitation in the Southern Alps of New Zealand—A case study. *Journal of Applied Meteorology*, 36 (5), pp.428-442.
- Stoelinga, M.T., Stewart, R.E., Thompson, G. and Thériault, J.M., 2013. Microphysical processes within winter orographic cloud and precipitation systems. In *Mountain Weather Research and Forecasting* (pp. 345-408). Springer, Dordrecht.
- Waldteufel, P. and Corbin, H., 1979. On the analysis of single-Doppler radar data. *Journal of Applied Meteorology and Climatology*, 18 (4), pp.532-542.
- Wratt, D.N., Ridley, R., Sinclair, M.R., Larsen, H.M., Thompson, S., Henderson, R., Austin, G., Bradley, S.H., Auer, A., Sturman, A.F., Owens, I., Fitzharris, B., 1996. The New Zealand Southern Alps Experiment. *Bulletin of the American Meteorological Society*, 77, pp 683-692.